AGU PUBLICATIONS

JGR

Journal of Geophysical Research: Atmospheres

RESEARCH ARTICLE
10.1002/2017JD026652

Key Points:
- Observed changes in SCF are highly correlated with anomalies in a_s and streamflow observed at multiple gauging stations over the TP
- An enhanced S_nRF on the TP is found in the long term from 1982 to 2014, but this cooling effect weakened during 2001-2014
- Intra-annual variability in S_nRF has intensified during the snow accumulation season but weakened in the melt season

Correspondence to:
D. Long,
dlong@tsinghua.edu.cn

Citation:
Chen, X., D. Long, Y. Hong, S. Liang, and A. Hou (2017), Observed radiative cooling over the Tibetan Plateau for the past three decades driven by snow cover-induced surface albedo anomaly, *J. Geophys. Res. Atmos.*, *122*, 6170–6185, doi:10.1002/2017JD026652.

Received 14 FEB 2017
Accepted 24 MAY 2017
Accepted article online 30 MAY 2017
Published online 21 JUN 2017

Observed radiative cooling over the Tibetan Plateau for the past three decades driven by snow cover-induced surface albedo anomaly

Xiaona Chen[1], Di Long[1], Yang Hong[1], Shunlin Liang[2], and Aizhong Hou[3]

[1]State Key Laboratory of Hydroscience and Engineering, Department of Hydraulic Engineering, Tsinghua University, Beijing, China, [2]State Key Laboratory of Remote Sensing Science, School of Geography, Beijing Normal University, Beijing, China, [3]Bureau of Hydrology, Ministry of Water Resources of the People's Republic of China, Beijing, China

Abstract Seasonal snow cover on the Tibetan Plateau (TP) is a sensitive indicator of climate change. Unlike the decreasing snow cover extent and associated weakening of radiative cooling effects for the Northern Hemisphere during recent decades reported by previous studies, snow cover variability over the TP and its impact on the energy budget remain largely unknown. We defined the snow cover-induced radiative forcing (S_nRF) as the instantaneous perturbation to Earth's shortwave radiation at the top of the atmosphere (TOA) induced by the presence of snow cover. Here using satellite observations and a radiative kernel approach, we found slightly enhanced S_nRF, i.e., a radiative cooling effect on the TP during the past three decades (1982–2014). However, this cooling effect weakened during 2001–2014 because of reduced snow cover at a rate of -0.61% decade^{-1} and land surface albedo at a rate of -0.72% decade^{-1}. Changes in snow cover fraction are highly correlated with anomalies in land surface albedo (a_s) over the TP both spatially and temporally. Moreover, the S_nRF is closely related to the direct observation of TOA shortwave flux anomalies ($R^2 = 0.54$, $p = 0.004$) over the TP during 2001–2014. Despite the insignificant interannual variability in S_nRF, its intra-annual variability has intensified driven mostly by enhanced S_nRF during the snow accumulation season but weakened S_nRF during the melt season, indicating greater energy release during the transition between accumulation and melt seasons. This may pose a great challenge to snow meltwater use and flood prediction for transboundary rivers originating from the TP, such as the Brahmaputra River basin.

Plain Language Summary Despite many earlier related studies, snow cover variability and its effect on the energy budget for the Tibetan Plateau, as the Earth's third pole, remain largely unknown. In contrast to the generally accepted reduction over recent decades in the extent of snow cover in the Northern Hemisphere and the related decrease in radiative cooling effects reported in earlier works, using improved satellite observations, this study found enhanced radiative cooling over the Tibetan Plateau (TP) during 1982–2014, i.e., generally increased snow cover, particularly during the snow accumulation season. Improved understanding of such an effect is crucial to the sustainable utilization of snow meltwater and to the understanding of potential flooding risks over the lower reaches of the transboundary rivers originating on the TP.

1. Introduction

As Earth's third pole and with the highest midlatitude mountains in the Northern Hemisphere (NH), the Tibetan Plateau (TP) has received considerable attention from the climate change community [*Larson*, 2011; *Yao et al.*, 2012]. Snow cover change over the TP is one of the primary topics because of its role in Earth's energy balance and its importance to snow meltwater-fed rivers. At continental scales, snow cover has important linkages with anomalies in climate system and snow-albedo feedbacks to temperature through its influence on global surface energy and moisture fluxes, clouds, precipitation, hydrology, atmospheric circulation [*Chen et al.*, 2015; *Frei et al.*, 2012; *Hall et al.*, 2008], and climatic anomalies, e.g., vegetation phenology [*Dong et al.*, 2013], monsoons [*Boos and Kuang*, 2010], river sediment [*Nie et al.*, 2015], livelihoods [*Haynes et al.*, 2014], and land surface heat fluxes [*Ma et al.*, 2006]. Without snow cover, the ground absorbs about 4 to 6 times more of the Sun's energy. Thus, the presence or absence of snow controls patterns of heating

and cooling over Earth's land surface more than any other single land surface feature. Moreover, snow cover is an important indicator of climate variability, particularly changes in temperature and precipitation [*Chen et al*., 2016b]. In addition, the shrinkage of snow cover extent results in reduced reflection of solar radiation and leads to rising land surface temperatures [*Qu and Hall*, 2014]. At regional scales, snow cover on the TP has considerable potential to influence the regional hydrological cycle and may affect the frequency of heat waves in northern China [*Wu et al*., 2012] and to contribute to changes in vegetation greenness onset [*Dong et al*., 2013], the East Asian summer monsoon [*Pu et al*., 2008] and atmosphere-land interaction [*Ma et al*., 2009]. Furthermore, seasonal snow cover across the TP constitutes vital storage of surface water for Southwest China and neighboring countries. The major rivers of China and the surrounding Asian countries, including the Yellow, Yangtze, Mekong, Brahmaputra, and Indus Rivers, all originate on the TP.

The snow cover in the TP is not only one of the main snow cover areas in China but also one of the most important components of the NH cryosphere. Previous studies have shown that snow cover in the NH has experienced a well-documented and rapid decrease since the late 1960s [*Brown and Robinson*, 2011; *Derksen and Brown*, 2012], and climate projections suggest that snow cover will continue to reduce in the future [*Brown and Robinson*, 2011; *Intergovernmental Panel on Climate Change*, 2013], coincident with hemispheric warming and the positive feedback of surface reflectivity on climate [*Brown et al*., 2010; *Brown and Robinson*, 2011; *Flanner et al*., 2011]. However, because of decreased winter temperatures and enhanced midlatitude westerlies [*Mölg et al*., 2013], snow cover in midlatitude regions has shown increased extent with delayed snow end dates and prolonged snow durations during 2001–2014 [*Chen et al*., 2015]. Compared with other midlatitude regions, seasonal snow cover over the TP has unique features in terms of global snow cover map because of the high mountains and it has vital water storage properties [*Pu et al*., 2007]. With an accelerated change in the environment on the TP caused by climate change [*Zhong et al*., 2011], including anomalies in warming trend [*Duan and Xiao*, 2015], advanced vegetation green-up dates [*Zhang et al*., 2013], enhanced evaporative cooling [*Shen et al*., 2015], and shrinking glaciers [*Chen et al*., 2017; *Long et al*., 2017; *Yao et al*., 2012] in most regions over the TP, the status of snow cover and its contribution to the Earth climate system remain unknown.

Given the importance of snow cover over the TP, a number of studies have quantified snow cover conditions in the TP and explored its response to climate change in recent decades [*Lau et al*., 2010; *Pu et al*., 2007, 2008; *Wang et al*., 2013; *Wu et al*., 2012; *Zhang et al*., 2004], e.g., seasonal variations in snow cover fraction (SCF) [*Pu et al*., 2007; *Wu et al*., 2012; *Wang et al*., 2013], decadal changes in spring snow depth [*Zhang et al*., 2004], and snow melt conditions in the western TP and Himalayas [*Lau et al*., 2010]. However, few of the above mentioned studies have quantified the impacts of snow cover changes on the Earth's energy budget due to complex terrain, highly spatial heterogeneity in snowfall and snow cover distribution, poor quality of snow cover and land surface albedo (a_s) data sets, and few in situ observations across the TP [*Tang et al*., 2017].

The objectives of this study are therefore to (1) examine variations in snow cover, surface albedo a_s (including the albedo of snow and other land cover types), and snow-free albedo (a_{sf}, mainly reflecting the albedo of vegetation) over the TP; (2) quantify the contributions of snow-covered and snow-free surfaces to the snow-induced albedo contrast (Δa_s, i.e., a_s minus a_{sf}); (3) estimate the instantaneous perturbation to Earth's shortwave radiation at the top of the atmosphere (TOA) induced by the presence of snow cover (S_nRF) using a radiative kernel method and compared with satellite-observed TOA shortwave radiation anomalies from 2001 to 2014; and (4) estimate S_nRF for the period 1982–2014 to investigate how snow cover changes affect TOA shortwave radiation over the TP in the long term.

2. Data and Method

2.1. Study Area

TP regions are sources of several major rivers, e.g., the Yangtze River, Yellow River, Mekong River, and the upper reaches of the Brahmaputra River and Indus River, of China and surrounding Asian countries. The topography over the TP is complex, and examining snow cover can be difficult because complex terrain results in considerable spatial variations within the footprint of remotely sensed snow depth, surface characteristics, and satellite viewing angles. The location of TP is shown in Figure 1.

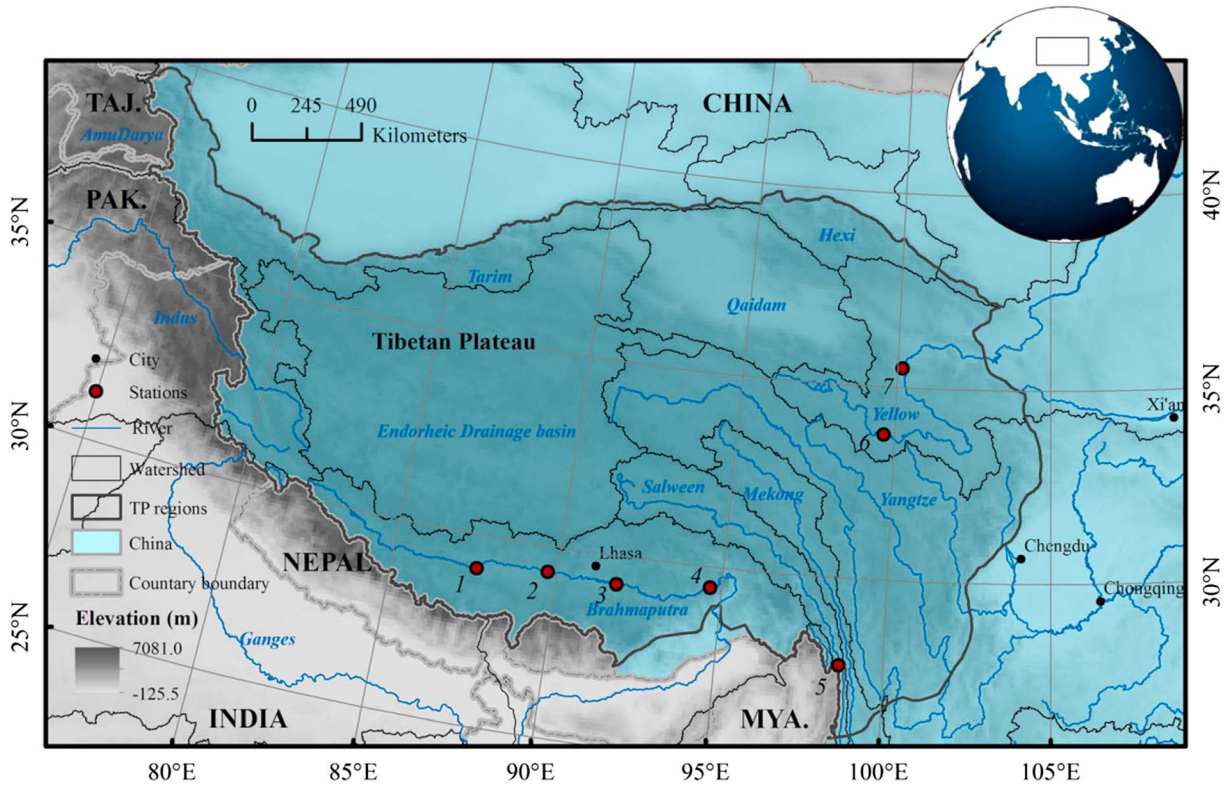

Figure 1. The TP and its surrounding regions. Illustrated are the distributions of major rivers, watershed boundaries (i.e., AmuDarya, Indus, Ganges, Brahmaputra, Salween, Mekong, Yangtze, Yellow, and Hexi), endorheic drainage basins (i.e., Tarim, Inner TP, and Qaidam), streamflow gauges, associated countries, and elevations. Details of the streamflow gauges are listed in Table 2.

Considering the fluctuation of snow cover over different years, we confined the study area to extensive snow-covered regions over the TP where snow covers the ground for at least 8 weeks (about 60 days) in 75% of the years, following *Liu and Chen* [2011]. To explore the snow cover changes in the accumulation season and melt season, we used hydrological year from September of one year ($t-1$) to August of the following year (t) based on the annual cycle of SCF averaged over the entire TP with elevation above 2000 m [*Pu et al.*, 2007]. Moreover, we defined the accumulation season of snow cover over the TP as September of one year ($t-1$) to next February of the following year (t) and melting season over the TP as March to August in one year (t) in this study.

2.2. Data Sets

2.2.1. Snow Data Set

Satellite remote sensing has been used to map and monitor snow cover for more than 40 years [*Brown et al.*, 2010; *Frei et al.*, 2012], using tools such as the binary daily snow cover mask derived from the Interactive Multisensor Snow and Ice Mapping System [*Helfrich et al.*, 2007], the Northern Hemisphere Weekly Snow Cover and Sea Ice Extent [*Helfrich et al.*, 2007; *Robinson et al.*, 1993], the Moderate Resolution Imaging Spectroradiometer Satellite (MODIS) snow cover products [*Hall et al.*, 1995], and the Advanced Microwave Scanning Radiometer-Earth Observing System (AMSR-E) snow water equivalent (SWE) products [*Kelly et al.*, 2003]. However, limited by complex topography, heterogeneous land cover types, scattered snow cover distributions, and relatively low spatial and temporal resolutions of images, few of these products are well suited for snow cover study over the TP.

To investigate snow cover across the TP at the highest available spatial and temporal resolutions, we used optical remote sensing-derived snow cover data collected over the TP during 2001–2014 from the improved MODIS daily snow cover data set (MCD10A1-TP), which was integrated by *Huang et al.* [2014] using MODIS Terra/Aqua daily snow cover products (MOD10A1 and MYD10A1) and passive microwave AMSR-E daily SWE products. By combining optical and passive microwave snow cover products, the overall classification

Table 1. Details of Gridded Data Sets Used in This Study

Variables	Data Sets	Horizontal Resolution	Temporal Resolution	Time Span	References
Snow cover	MCD10A1-TP	500 m	Daily	2001–2014	*Huang et al.* [2014]
Albedo	GLASS	0.05°	8 day	1981–2014	*Liang et al.* [2013a]
	MCD43GF	0.0083°	8 day	2001–2014	*Moody et al.* [2008]
Radiative flux	CERES	1°	Monthly	2001–2014	*Wielicki et al.* [1996]
Radiative kernels	CAM3	2.5°	Monthly	–	*Shell et al.* [2008]
	AM2	2.5°	Monthly	–	*Soden et al.* [2008]

accuracy of the MCD10A1-TP reaches 91.7% when snow depth is over 3 cm, suggesting that the MCD10A1-TP is suitable for monitoring snow cover changes in the TP.

2.2.2. Land Surface Albedo Data Set

To quantify Δa_s applied to estimate the S_nRF, the Global Land Surface Satellite (GLASS) a_s product [*Liang et al.*, 2013a] during 1981–2014 and the MODIS-derived global gap-filled snow-free bidirectional reflectance distribution function/albedo (MCD43GF) data sets [*Moody et al.*, 2008] during 2001–2014 were used in this study. GLASS a_s is the land surface albedo, and MCD43GF a_s is snow-free albedo a_{sf}. Thus, we obtained yearly and monthly Δa_s time series by subtracting MCD43GF a_{sf} from GLASS land surface a_s in the corresponding period.

Currently, data sets from the Advanced Polar Pathfinder (APP-X), MODIS, International Satellite Cloud Climatology Project, Satellite Application Facility on Climate Monitoring advanced very high resolution radiometer (AVHRR) clouds, albedo, and radiation first release (CLARA-A1-SAL), and Global Land Surface Satellite (GLASS) are the only available long-term satellite-derived a_s products. The GLASS a_s, produced from both AVHRR and MODIS data [*Liang et al.*, 2013a], has been used to quantify the radiative forcing of snow melting over Greenland [*He et al.*, 2013] as well as changes in snow cover phenology over the Northern Hemisphere (NH) [*Chen et al.*, 2016a, 2015]. Compared with other data sets, GLASS is ideal for S_nRF estimation because of its fine spatial resolution (1 km and 0.05°), long time span (1981–2014), and spatially complete properties [*Liang et al.*, 2013a, 2013b] that may reduce uncertainties in the quantification of snow-induced Δa_s.

2.2.3. Radiative and Radiative Kernel Data Sets

To quantify the S_nRF and its impact on the energy budget, both the radiative kernel method [*Shell et al.*, 2008; *Soden et al.*, 2008] and the Clouds and the Earth's Radiant Energy System (CERES) satellite products [*Wielicki et al.*, 1996] during 2001–2014 were used in this study. The radiative kernel approach allows us to separate the radiative responses to different climate parameters (e.g., albedo a_s, temperature, water vapor, and CO_2) and to decompose the feedback into radiative and climate response components. The radiative kernel approach was used to evaluate S_nRF. The CERES observations were used to explore the contribution of S_nRF in total TOA shortwave anomalies. In order to compare S_nRF with TOA shortwave anomalies, we employed the CERES Energy Balanced and Filled (EBAF) product. The CERES EBAF data set provides spatially complete, clear-sky TOA flux climatology for each 1° region every month [*Loeb et al.*, 2009].

The albedo radiative kernels, expressed as the TOA shortwave flux anomalies associated with a 1% change in land surface a_s, were used to estimate S_nRF. The albedo radiative kernels originally provided at 2.5° resolution, using offline radiative transfer codes from the Community Atmosphere Model version 3 (CAM3) as described by *Shell et al.* [2008] and the Atmosphere Model 2 (AM2) as demonstrated by *Soden et al.* [2008], were used in this study. Compared with the analytical models, the radiative kernel methods are more accurate because they more effectively capture the functional dependence of planetary albedo on a_s [*Qu and Hall*, 2014].

Details of gridded data sets used in this study are listed in Table 1. To match the temporal resolution of monthly albedo radiative kernels, the daily MCD10A1 over the TP was aggregated to produce a monthly averaged SCF series, in which the SCF was defined as the number of days with snow observations in a month divided by the total number of days in a month. The quality control flags of "00" and "01" of GLASS land surface a_s, indicating uncertainties of $<5\%$ and $<10\%$, were used to generate the monthly mean land surface a_s values. Quality assurance values between "0" and "1" of MCD43GF a_{sf}, representing the majority of

Table 2. Details of the Streamflow Gauges Used in This Study

Number	Name	River	Latitude (°N)	Longitude (°E)
1	Lazi	Brahmaputra	29.12	87.58
2	Nugesha	Brahmaputra	29.32	89.71
3	Yangcun	Brahmaputra	29.27	91.82
4	Nuxia	Brahmaputra	29.47	94.65
5	Gongshan	Salween	27.73	98.68
6	Jimai	Yellow	33.77	99.65
7	Tangnaihai	Yellow	35.5	100.15

high-quality full inversion values, were used to generate the monthly mean a_{sf} and climatology a_{sf}. Before calculation, all of the data sets used in this study were regridded at a spatial resolution of 0.05° in a geographic latitude/longitude projection.

2.2.4. Streamflow Data Set

To validate changes in SCF, this study also employed streamflow gauges on the TP. Details of these gauges distributed in the Brahmaputra, Yellow, and Salween Rivers are provided in Table 2.

2.3. Methods

2.3.1. Attribution Analysis

Attribution analysis was used to investigate the contributions from snow and snow-free surfaces to Δa_s anomalies over the TP during 2002–2014. To consistently quantify the contributions of changes in a_s and a_{sf} to Δa_s, both a_s and a_{sf} were converted into standardized z-score anomalies using the mean and standard deviation of each time series between 2002 and 2014. The standard score of a raw score x [*Kreyszig*, 1979] is

$$z = \frac{x - \mu}{\sigma} \tag{1}$$

where μ is the mean of a_s, a_{sf}, or Δa_s over the TP during the period 2002–2014; σ is the standard deviation of a_s, a_{sf}, or Δa_s in the corresponding period. Then, the z-scores of the Δa_s time series were regressed against those of the a_s and the a_{sf} time series. The resulting regression coefficients were multiplied by the time series of a_s and a_{sf} z-scores to derive the relative contributions of a_s and a_{sf} to Δa_s variability.

2.3.2. S_nRF Estimation

The radiative kernel method is widely used in estimation of radiative forcing induced by changes in the cryosphere, such as sea ice [*Cao et al*., 2015; *Flanner et al*., 2011] and snow cover [*Chen et al*., 2015]. The time (t) dependence of S_nRF (W m^{-2}), within a region R (here the TP) of area A, composed of grid cells r can be expressed as follows [*Chen et al*., 2015; *Flanner et al*., 2011]:

$$S_n\mathrm{RF}(t,R) = \frac{1}{A(R)}\int_R S(t,r)\frac{\partial a_s}{\partial S}(t,r)\frac{\partial F}{\partial a_s}(t,r)\mathrm{d}A(r) \tag{2}$$

where S is the domain of snow cover over the TP, $\partial\alpha_s/\partial S$ is the rate of variation of a_s with snow cover change, and $\partial F/\partial\alpha_s$ is the response of TOA net shortwave radiation anomalies to a_s changes. We assumed that the temporally and spatially varying $\partial\alpha_s/\partial S$ and $\partial F/\partial\alpha_s$ are constant with snow cover fraction S and α_s, respectively. Then, $\partial\alpha_s/\partial S$ can be replaced with the mean Δa_s induced by the snow cover anomaly and $\partial F/\partial\alpha_s$ can be obtained from the albedo radiative kernels [*Chen et al*., 2015; *Flanner et al*., 2011]. To reduce uncertainty in S_nRF estimation, we averaged two S_nRF results using CAM3 and AM2 albedo radiative kernels to obtain the mean S_nRF values over the TP.

3. Results and Discussion

In order to estimate long-term S_nRF and address the lack of fine spatial resolution snow cover maps prior to 2001, we first quantified SCF anomalies over the TP from 2001 to 2014. Then, we calculated albedo contrast

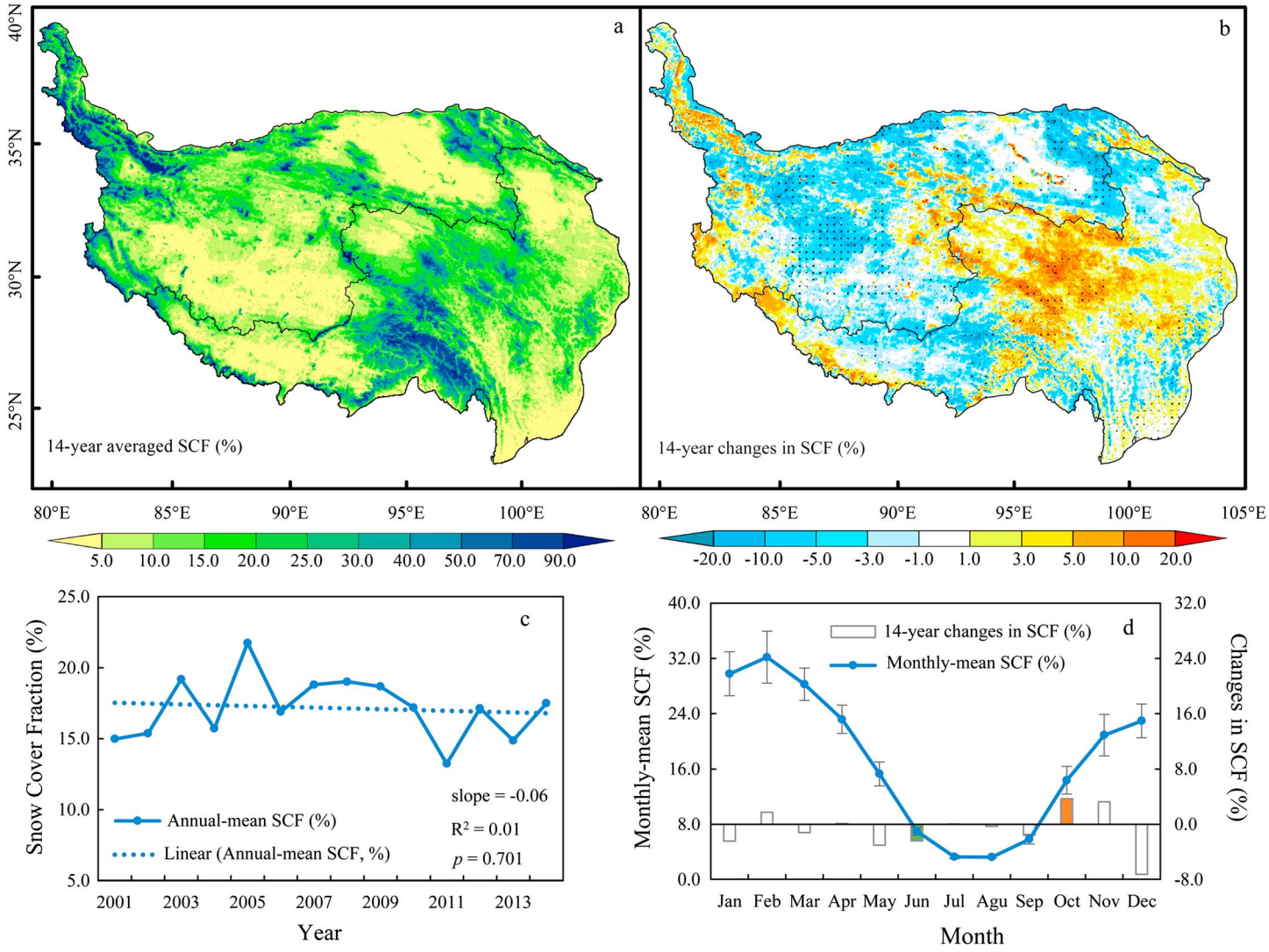

Figure 2. The 14 year (a) annual mean SCF, (b) changes, (c) interannual variability in annual mean SCF and linear trend in SCF, and (d) intra-annual variability in monthly mean SCF and 14 year changes of SCF in each month during 2001–2014 over the TP. Black dots in Figure 2b indicate that changes are statistically significant at the 95% level. The orange (green) color indicates an increase (decrease) in SCF in a given month from 2001 to 2014. The error bar in Figure 2d is expressed as the standard deviation of SCF in a given month during 2001–2014.

Δa_s caused by snow cover changes, as well as its contributions from the snow cover and snow-free land surfaces, and explored the magnitude of S_nRF in total TOA shortwave anomalies during 2001–2014. Finally, based on the correlation between snow cover and a_s, satellite observations, and the radiative kernel approach, this study estimated long-term S_nRF for the period 1982–2014.

3.1. Observed Snow Cover Changes From 2001 to 2014

Spatial distributions of annual mean SCF, changes, and interannual and intra-annual variability over the TP during 2001–2014 are shown in Figure 2. The changes are expressed as the slope of the line of linear regression multiplied by the study period.

The 14 year annual mean SCF over the TP from 2001 to 2014 was 17.16 ± 2.23%. High SCF values are distributed mainly in the upper reaches of the Tarim River, Brahmaputra River, and Mekong River basins, and low SCF values are distributed in the Inner TP and Qaidam River basins (Figure 2a). The 14 year changes in SCF show large spatial heterogeneity over the study area, in which the SCF generally decreases over the entire TP (Figure 2c), particularly the southeast TP around 25°N and Inner TP endorheic drainage basin around 35°N. In

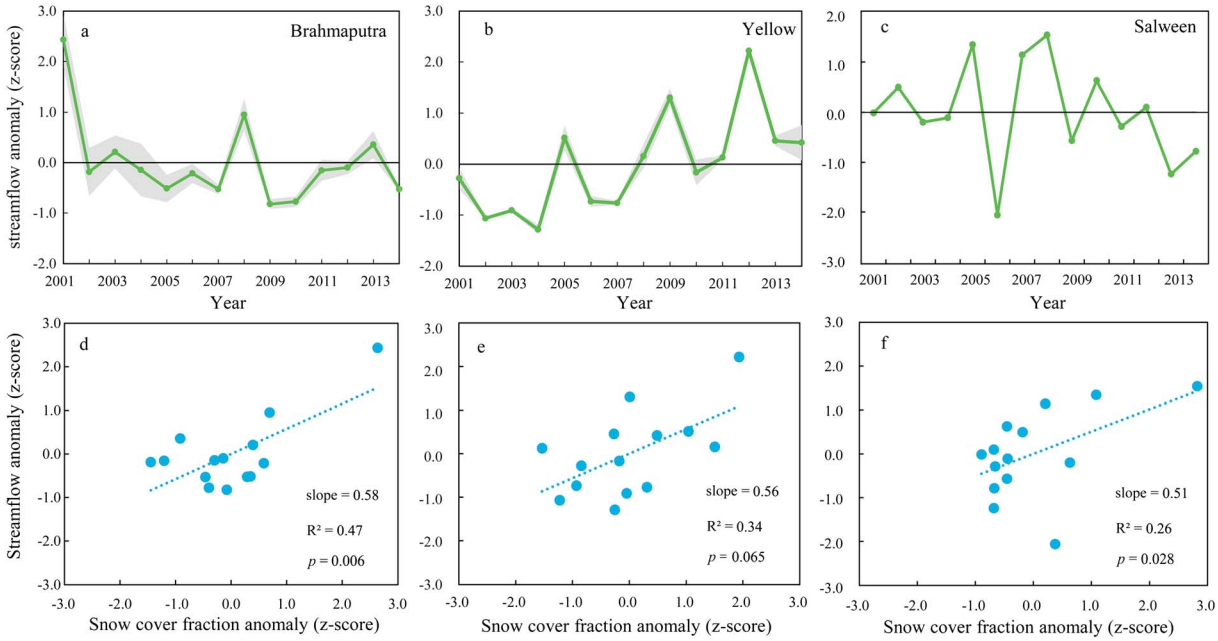

Figure 3. Observed streamflow changes in the melt season during 2001–2014. Mean streamflow anomalies in May and June for the period 2001–2014 in the upper reaches of the (a) Brahmaputra, (b) Yellow, and (c) Salween Rivers. Linear correlations between the observed streamflow anomaly and snow cover fraction anomaly in the (d) Brahmaputra, (e) Yellow, and (f) Salween Rivers. Shaded areas in Figure 3a are the standard deviation of streamflow observed at four gauges along the upper reaches of the Brahmaputra River. Shaded areas in Figure 3b are the standard deviation of streamflow observed at two gauges along the upper reaches of the Yellow River.

contrast to the SCF decrease in the Brahmaputra and Salween River basins, the SCF increases significantly in the upper reaches of the Yangtze and Mekong River basins, the upper reaches of the Brahmaputra River basin, and the Pamirs as displayed in Figure 2b. Compared with the decreased SCF in the accumulation season (−0.43%, p = 0.806), the SCF reductions during the melt season are more significant (−1.14%, p = 0.552), particularly in June (−2.42%, p = 0.017). The increased SCF in the snow accumulation season but decreased SCF in the snow melt season may cause more snow cover to be released as meltwater during the transition period between accumulations and melt seasons over the TP.

As the solid storage of surface water for several rivers, snow cover anomalies are highly correlated with streamflow over the TP. To cross validate the changes in SCF, the streamflow changes of the Brahmaputra, Salween, and Yellow Rivers in the melt season during 2001–2014 are shown in Figure 3.

The anomalies in SCF coincide markedly with observed changes in streamflow over the TP, e.g., decreased streamflow in the upper reaches of the Brahmaputra (Figure 3d, p = 0.006) and Salween Rivers (Figure 3f, p = 0.028) and increased streamflow in the upper reaches of the Yellow River (Figure 3e, p = 0.065) during the melt season (May and June) for the period 2001–2014, which spatially coincides with the observed remarkably decreased SCF at the pixel location of gauges distributed in the Brahmaputra and Salween River basins, as well as increased SCF at the pixel location of gauges distributed in the Yellow River basin.

3.2. Observed Changes in Surface Albedo and Snow-Free Surface Albedo

Previous studies by *Flanner et al.* [2011] and *Chen et al.* [2015] calculated the albedo contrast Δa_s induced by snow cover anomaly by subtracting a_{sf} climatology from a_s. However, Δa_s calculated by this approach does not consider snow-free surface variability (mainly vegetation type). The contribution analysis was used to investigate the contribution from snow and snow-free surfaces to Δa_s quantification prior to using this approach. Limited by the availability of the a_{sf} prior to 2001, attribution analysis was carried out for snow seasons from 2002 to 2014 as displayed in Figure 4.

Compared with the 13 year annual mean a_{sf} (Figure 4b), the 13 year annual mean land surface a_s shows relatively higher values in the northwest and southeast TP (Figure 4a), which is highly similar to the spatial distribution of SCF presented in Figure 2a. Moreover, changes in albedo contrast Δa_s (Figure 4e) are highly

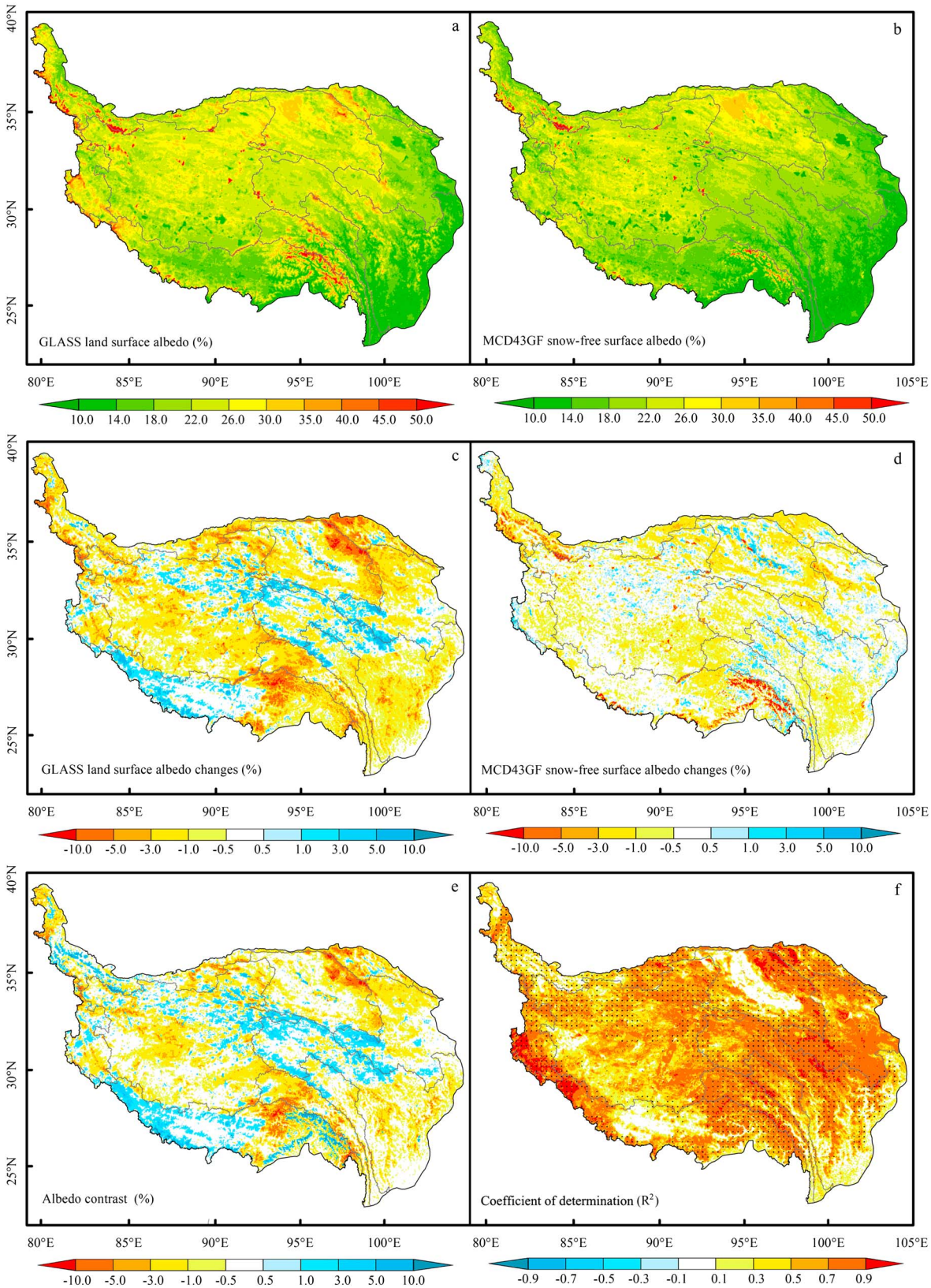

Figure 4. The 13 year annual mean (a) land surface albedo (a_s), (b) a_{sf}, changes in (c) a_s, (d) a_{sf}, and (e) albedo contrast (Δa_s) between a_s and a_{sf}, and (f) coefficient of determination (R^2) between snow cover fraction (SCF) and Δa_s over the TP during 2002–2014. Black dots in Figure 4f indicate that the linear correlation between SCF and Δa_s is statistically significant at the 95% level.

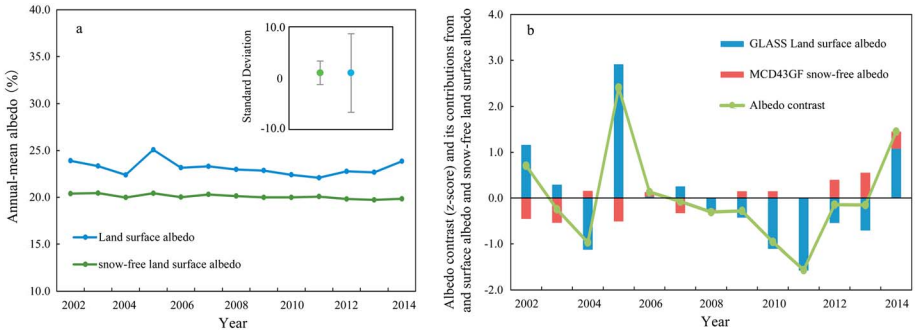

Figure 5. (a) Interannual variability and standard deviation in a_s and a_{sf} and (b) contributions from a_s and a_{sf} in Δa_s calculation in each month over the TP during 2002–2014.

consistent with changes in SCF in the corresponding period. The correlation coefficients between SCF and Δa_s over the TP during 2002–2014 are above 0.7 over 86% of the study area (Figure 4f), indicating that Δa_s is determined primarily by changes in surface a_s (Figure 4c) instead of by a_{sf} (Figure 4d). In response to the increase in SCF, a_s increases due to higher reflectance of snow cover, resulting in more energy reflected by the surface. Meanwhile, decreases in SCF observed in the TP margin resulted in decreases in a_s, weakening the radiative cooling effects of snow cover.

Detailed variability in a_s and a_{sf} and its contributions in Δa_s in each year over the TP during 2002–2014 are shown in Figure 5. To consistently quantify the contributions of changes in a_s and a_{sf} to Δa_s, both a_s and a_{sf} were converted into standardized *z*-score anomalies according to equation (1). Compared with the interannual variability in a_s, a_{sf} anomalies are slightly over the TP from 2002 to 2014 (Figure 5a). The standard deviation in a_{sf} is 0.22% over the TP from 2002 to 2014, only approximately one third the standard deviation of a_s (0.76%) during the corresponding period. The contributions of a_s and a_{sf} anomalies were computed annually to reveal their changing influence on the underlying Δa_s variability. Moreover, as displayed in Figure 5b, the overall changes in a_{sf} account for 2.51% of a_s variability over the TP from 2002 to 2014. In addition, the differences between S_nRF estimates using a_{sf} derived from the MCD43GF data set and the climatology of a_{sf} are presented in Figure A1. The differences (0.15 W m^{-2}) between 13 year annual mean S_nRF using different a_{sf} account for 1.47% of 13 year averaged S_nRF over the TP during 2002–2014. Differences between S_nRF estimation using a_{sf} and the climatology of a_{sf} are shown in Figure A1. Based on Figures 5 and A1, using the climatology of a_{sf} will not influence the main conclusions of this study. Thus, to address the unavailability of a_{sf} prior to 2001 in S_nRF estimation, we used a_{sf} climatology during 2002–2014 in this study.

3.3. S_nRF Estimation Over the TP From 2001 to 2014

3.3.1. S_nRF Estimation Using Radiative Kernel Approach

Applying the radiative kernel approach with equation (2), spatial distributions of the 14 year annual mean S_nRF under clear-sky conditions and those changes during 2001–2014 are shown in Figure 6.

The 14 year annual mean S_nRF was estimated at −10.25 (±0.10) W m^{-2} over the TP for the period 2001–2014. Large negative values of clear-sky S_nRF are distributed mainly in the portion of the Brahmaputra River basin in the southeast TP and the Pamirs (Figure 6a) because of the high annual mean SCF values in these regions, as shown in Figure 2a. In accord with changes in SCF (Figure 2b), S_nRF enhanced (i.e., negatively increased) in the upper basins of the Mekong, Yangtze, and Yellow Rivers and the upper basin of the Brahmaputra River in the southwest TP, whereas weakened S_nRF (i.e., positively increased) in the portion of the Brahmaputra River basin in the southeast TP (Figure 6b). Driven by the general decreasing trend in SCF (Figure 2c), the annual mean S_nRF has weakened at a rate of 0.98 W m^{-2} $decade^{-1}$ (p = 0.46, Figure 6c) over the TP from 2001 to 2014, in which the maximum and minimum magnitudes of S_nRF occurred in 2005 and 2011, corresponding to the extreme low-temperature event in 2005 and the extreme drought in 2011 [*Long et al.*, 2014].

3.3.2. Direct Estimates of TOA Shortwave Flux Anomalies

Direct estimates of TOA shortwave radiation anomalies over the TP from 2001 to 2014 using CERES EBAF observations are shown in Figure 7, which further highlights the contribution of SCF to TOA shortwave anomalies over the TP.

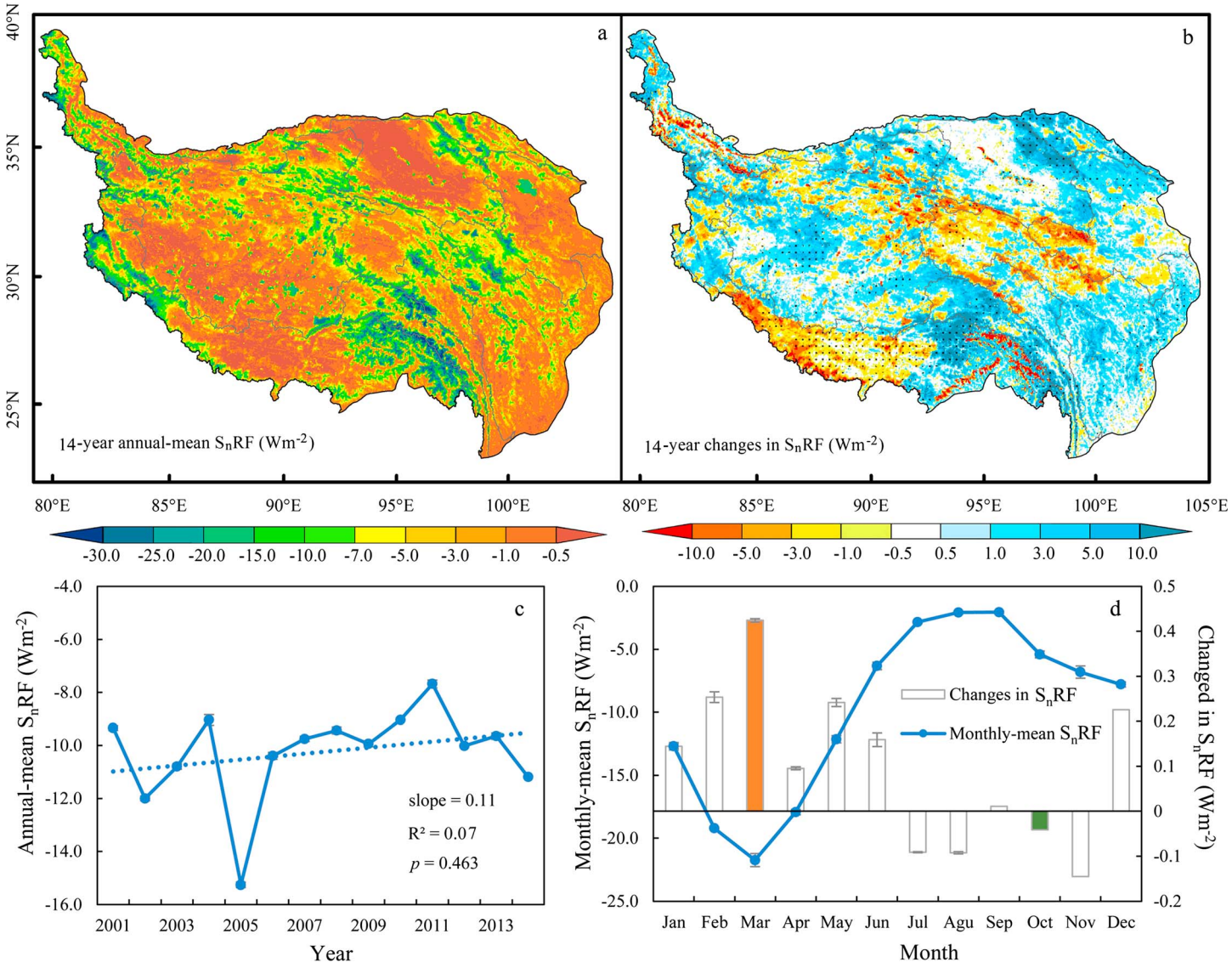

Figure 6. The 14 year (a) annual mean S_nRF, (b) changes, (c) interannual variability of annual-averaged S_nRF and linear trend in S_nRF, and (d) intra-annual variability of monthly averaged S_nRF and 14 year changes of S_nRF in each month over the TP from 2001 to 2014. Black dots in Figure 6b indicate that changes are statistically significant at the 95% level. The error bars in Figures 6c and 6d are expressed as the range derived from the two S_nRF results. The solid green bar in Figure 6d indicates that S_nRF was enhanced, and the changes are significant at the 95% level in a given month.

The coefficient of determination of 0.54 (p = 0.004) between the SCF and the TOA shortwave flux anomalies over the TP from 2001 to 2014 (Figure 7h) indicates that snow cover changes are likely to have a larger impact on TOA shortwave radiation budget through changes in a_s over the TP. Dominated by positive shortwave anomalies in the upper basins of the Yangtze and Mekong Rivers, the net TOA flux registers negative changes over these regions, implying that as SCF increases, the reflected shortwave flux increases, leading to the decreasing TOA net flux in these regions (Figures 7a and 7d). By comparing the linear correlation between SCF and TOA shortwave (Figure 7h) and longwave (Figure 7i) fluxes, it can be found that changes in SCF influence the TOA shortwave flux (slope = 0.72 W m^{-2}) more than the longwave flux (slope = −0.22 W m^{-2}). In addition, the observed TOA shortwave flux changes are highly consistent both spatially and temporally with the observed SCF anomalies over the TP during 2001–2014, indicating that changes in SCF might further influence and control the local and regional energy budgets under the effects of climate change. In contrast to the close correlation between SCF and TOA shortwave flux, the correlations between the interannual SCF and TOA longwave (Figure 7i) and net flux (Figure 7g) are not statistically significant.

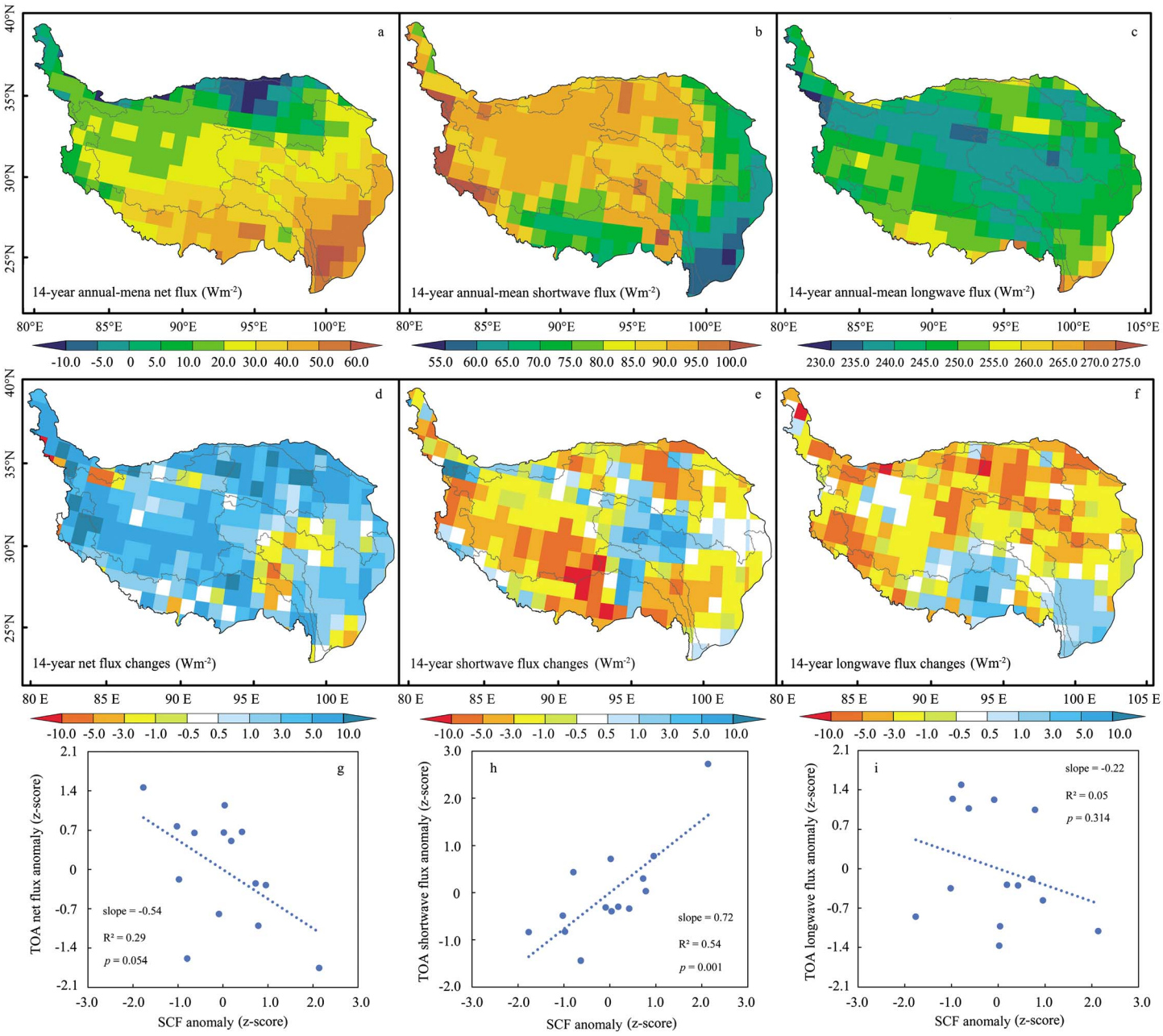

Figure 7. CERES-observed 14 year annual mean TOA (a) net flux, (b) shortwave flux, (c) longwave flux, and (d–f) corresponding changes over the TP from 2001 to 2014. The linear correlations between SCF and TOA (g) net flux, (h) shortwave flux, and (i) longwave flux over the TP from 2001 to 2014.

3.4. S_nRF Estimation Over the TP From 1982 to 2014

3.4.1. Observed Changed in Land Surface a_s Over the TP From 1982 to 2014

Quantifying the long-term a_s anomalies and Δa_s induced by snow cover changes is the key of S_nRF estimation. Changes in interannual and intra-annual a_s over the TP from 1982 to 2014 derived from the GLASS a_s data set are shown in Figure 8, and the climatology of changes in land surface a_s and a_{sf} in each month in this period is summarized in Table 3.

Due to the similarity of snow cover, ice, and cloud on optical remote sensing products, the accuracy of a_s products on snow cover and cloud is difficult to evaluate. The recent cross validation of satellite-retrieved a_s using GLASS a_s products and ground measurements taken by *He et al.* [2013] found that the GLASS a_s data

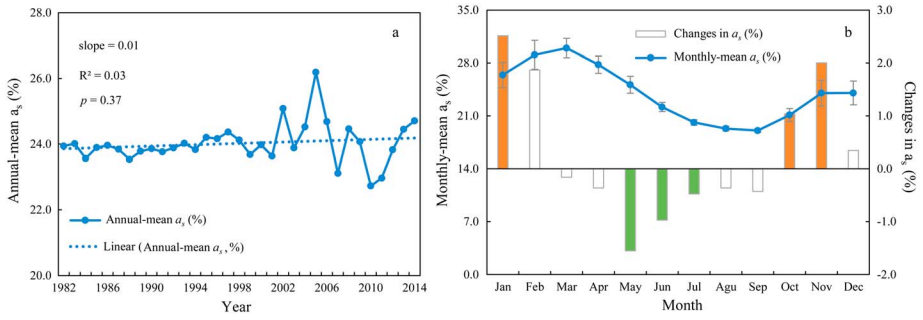

Figure 8. (a) Interannual and (b) intra-annual a_s changes over the TP from 1982 to 2014. The orange (green) color in Figure 8b indicates an increase (decrease) in a_s in a given month from 1982 to 2014. The error bar in Figure 8b is expressed as the standard deviation of a_s in a given month during 1982–2014.

can capture a_s changes temporally and spatially for Greenland with complex topography and snow distribution from 1982 to 2012. Therefore, in this study, we used GLASS a_s data over the TP from 1982 to 2014 directly without additional validation.

Results of the interannual variation in a_s over the TP reveal that land surface a_s generally increased at a rate of 0.89% decade^{-1} (p = 0.44) from 1982 to 2014, and fluctuated annually, reaching maximum and minimum values in 2005 and 2011, respectively (Figure 8a). However, the general trend of a_s over the TP is not statistically significant. The interannual correlation between the SCF from the Northern Hemisphere EASE-Grid 2.0 Weekly Snow Cover and Sea Ice data set [*Robinson et al*., 1993] and GLASS a_s is highly correlated with R^2 being 0.41($p < 0.001$) over the TP from 1982 to 2014 (Figure A2). Moreover, the intra-annual change in a_s over the TP shows an increasing trend in the accumulation season (October to the following February) but a decreasing trend in the melt season (May to September) from 1982 to 2014 (Figure 8b and Table 3). This coincides with the observed long-term tendency of increasing snow cover over the boreal regions since about the 1980s [*Chen et al*., 2016a; *Cohen et al*., 2012] and increasing temperatures in spring and summer over the TP [*Duan and Xiao*, 2015].

3.4.2. S_nRF Estimation From 1982 to 2014

Applying the radiative kernel approach with equation (2) in combination with GLASS a_s and the climatology of a_{sf} derived from MCD43GF, we estimated S_nRF over the TP from 1982 to 2014, as shown in Figure 9.

The 33 year annual mean S_nRF was estimated to be −9.86 (±0.11) W m^{-2} over the TP from 1982 to 2014 (Figures 9a and 9c), in which the 19 year annual mean S_nRF was estimated to be −9.57 (±0.11) W m^{-2} from 1982 to 2000, and the 14 year annual mean S_nRF was estimated to be −10.25 (±0.11) W m^{-2} from 2001 to

Table 3. Changes (%) in Land Surface Albedo a_s and a_{sf} in a Given Month During 1982–2014[a]

	1982–2000	2001–2014		1982–2014
Month	a_s	a_s	a_{sf}	a_s
Jan	0.56	−1.43	−0.62**	2.51**
Feb	0.91**	−0.05	−0.31	1.87*
Mar	0.25	−1.74	−0.20	−0.16
Apr	−0.34	−0.73	−0.14	−0.36
May	−0.37*	−1.47	−0.66***	−1.55**
Jun	0.10	−0.95*	−0.60**	−0.97***
Jul	−0.01	0.11	−0.65	−0.48**
Aug	0.38**	0.03	−0.70	−0.36
Sep	−0.02	−0.07	−0.83	−0.43**
Oct	0.12	0.04	−0.71**	1.04**
Nov	0.88*	0.02*	−0.76	2.01*
Dec	0.90	−1.98	−0.81	0.34

[a]Others are not significant at 90% level.
*Significance level: 90%.
**Significance level: 95%.
***Significance level: 99%.

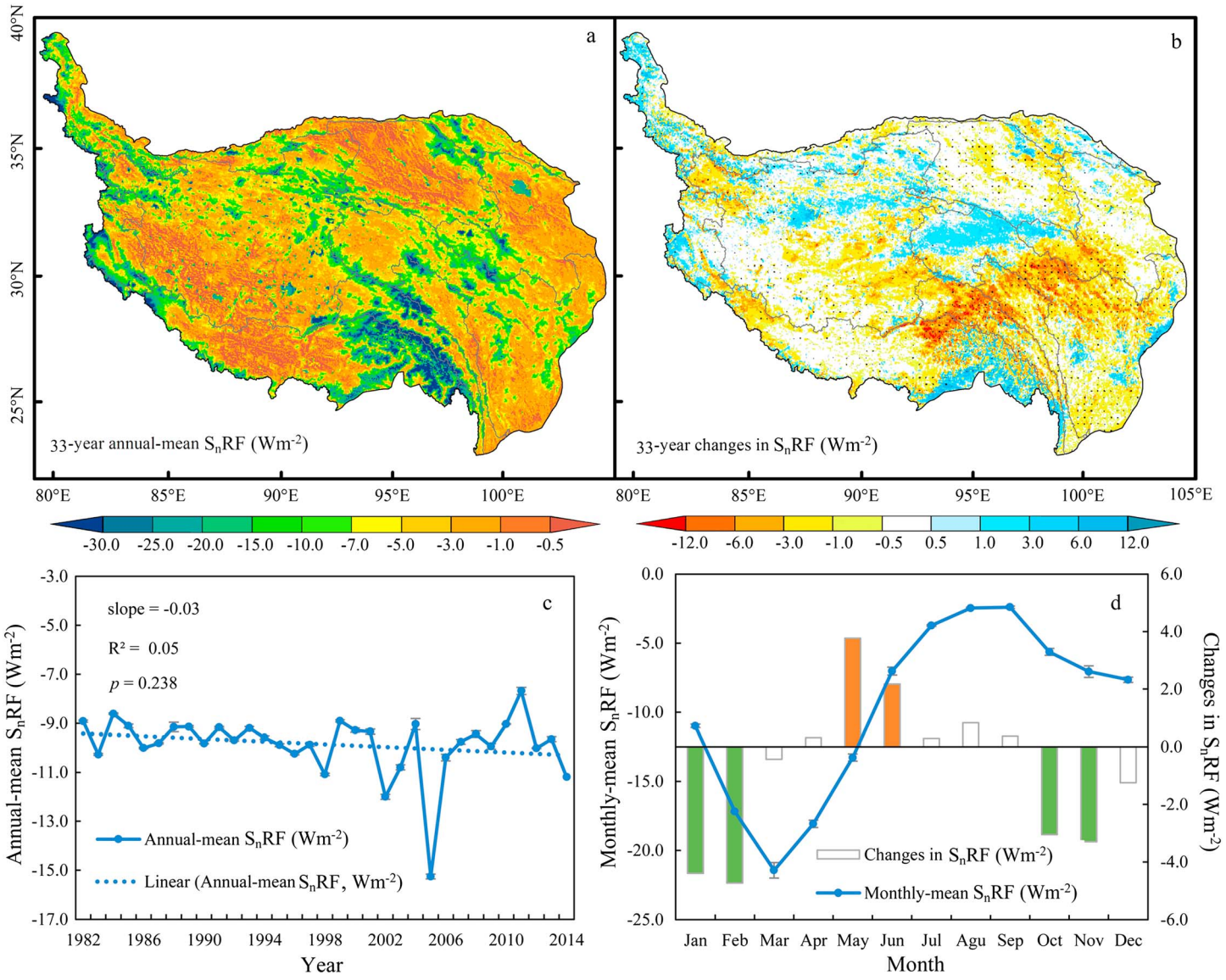

Figure 9. The 33 year (a) annual mean S_nRF, (b) changes, (c) interannual variability of annual-averaged S_nRF and linear trend in S_nRF, and (d) intra-annual variability of monthly averaged S_nRF and 33 year changes of S_nRF in each month over the TP during 1982–2014. The annual mean values in Figures 9a and 9c were averaged from two S_nRF results using CAM3 and AM2 kernels. The error bars in Figures 9c and 9d are expressed as the range derived from the two S_nRF results in clear-sky condition. Black dots in Figure 9b indicate that changes are statistically significant at the 95% level. The solid green bars in Figure 9d indicate that the S_nRF was enhanced, and the changes are significant at the 95% level in a given month over the TP during 1982–2014.

2014, indicating a generally increasing trend of radiative cooling over the TP from 1982 to 2014. Driven by the snow-induced a_s anomalies, the troughs of annual mean S_nRF occurred in 1998, 2002, and 2005, coincident with the large-scale El Niño phenomenon (i.e., 1998 and 2002) and the later onset of the vegetation growing season over the TP, particularly in 2005 [*Zhang et al.*, 2013]. Conversely, the peaks occurred in 1999, 2004, and 2011, corresponding to the La Niño phenomenon (i.e., 1999 and 2004) and the extreme drought in 2011 [*Long et al.*, 2014].

As shown in Figure 9a, regions with large magnitudes of S_nRF are distributed in the portion of the Brahmaputra River basin in the southeast TP. Driven by long-term a_s, S_nRF enhanced slightly over the TP from 1982 to 2014 (Figure 9c). Changes in S_nRF over the TP during 1982–2014 were estimated to be −0.91 (±0.02) W m^{-2}. As shown in Figure 9b, S_nRF over the southeast TP enhanced, except at the fringes of the Brahmaputra River basin. Meanwhile, S_nRF over the central and northern TP weakened during 1982–2014. The distribution of changes in S_nRF is determined primarily by anomalies in snow cover. In association

with the declining land surface temperatures in the snow accumulation season in the southern TP, precipitation increased in the upper basins of the Salween, Mekong, and Yangtze Rivers but decreased over the Himalaya. This resulted in an increase in SCF followed by a higher Δa_s and hence enhanced S_nRF in the upper basins of the Salween, Mekong, and Yangtze Rivers, whereas the converse occurred over the fringes of the Brahmaputra basin in the southeast TP.

The intra-annual cycles of S_nRF are shown in Figure 9d. S_nRF increases significantly (green bars) during September–February, indicating an enhanced radiative cooling effect during the snow accumulation season over the TP. However, S_nRF peaks at approximately -21.75 (± 0.52) W m^{-2} in March, when both solar irradiance and SCF over the TP are high. The earlier maximum SCF values over the TP, in comparison with the entire NH, mean that the peak of S_nRF over the TP is earlier than that for the entire NH (April), as described by *Flanner et al*. [2011]. Moreover, S_nRF weakens at 3.77 W m^{-2} ($p = 0.047$) in May and 2.18 W m^{-2} ($p = 0.022$) in June. Conversely, it enhances at -3.05 ($p = 0.003$), -3.29 ($p = 0.048$), -4.39 ($p = 0.005$), and -4.73 W m^{-2} ($p = 0.038$) in October, November, January, and February, respectively. Enhanced S_nRF in the accumulation season benefits snow accumulation, which would be conducive to the water supply to the areas of the lower reaches of the study river basins that depend, to a varying degree, on snow meltwater. However, risks might also be increased because of the enhanced possibility of snow meltwater-induced flooding in spring [*Arnell and Gosling*, 2016].

4. Concluding Remarks

Estimating long-term snow cover-induced radiative forcing S_nRF is vital for both climate change studies and future climate projections over the TP. Based on improved satellite observations, this study investigated the distribution of snow cover, land surface a_s, and a_{sf} changes over the TP and quantified S_nRF from 1982 to 2014.

Under the background of a large-scale winter cooling trend over the NH midlatitudes and an overall warming trend over the TP, a_s over the TP increased slightly from 1982 to 2014 and resulted, in general, enhanced S_nRF over the TP during the corresponding period. This coincides with the finding of *Flanner et al*. [2011], in which the TP is one of the few regions with enhanced S_nRF during 1979–2008 over the entire NH. In contrast to the insignificant interannual changes in S_nRF, intra-annual changes in S_nRF showed an enhanced trend in the accumulation seasons, as well as a weakened trend in the melting seasons. Different from increased SCF and snow duration days in NH midlatitudes [*Chen et al*., 2015], snow cover in the TP showed a decreasing trend within the context of generally increasing temperatures during 2001–2014. Despite the contrasting trends of large-scale winter cooling over NH midlatitudes and overall warming [*Cohen et al*., 2012, 2014], a_s over the TP increased slightly from 1982 to 2014. This resulted in a generally enhanced S_nRF and a radiative forcing cooling effect, particularly during the snow accumulation season. Moreover, intra-annual changes in S_nRF showed an enhanced trend in the accumulation season as well as a weakened trend in the melt season during the periods of 2001–2014 and 1982–2014, which coincides with observed changes in streamflow at multiple gauges in the southeast TP. It is very likely that the trend of warming and the enlarged intra-annual variation of S_nRF over the TP will continue. Therefore, monitoring, modeling, and prediction of snow cover and snow-induced flooding are urgently needed to utilize streamflow resources better and to reduce flooding risks over the TP region whose water resources sustain more than 1 billion people in Asia.

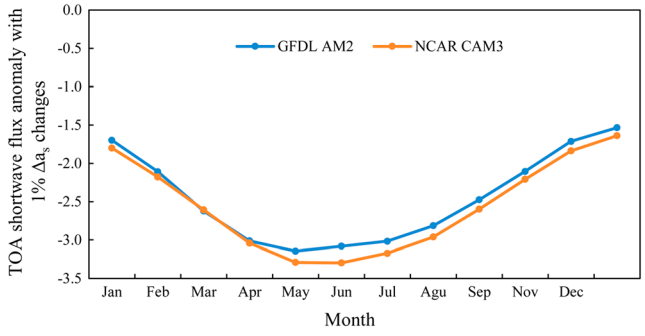

Figure A1. Differences between S_nRF estimation using snow-free albedo and the climatology of snow-free albedo.

Appendix A

The differences between S_nRF estimations using realistic a_{sf} and the climatology of a_{sf} are presented in Figure A1. The differences (0.15 W m^{-2}) between 13-year annual-mean S_nRF using different a_{sf} account for 1.47% of 13-year averaged S_nRF over the TP during 2002–2014. Thus, using the climatology of a_{sf} will not

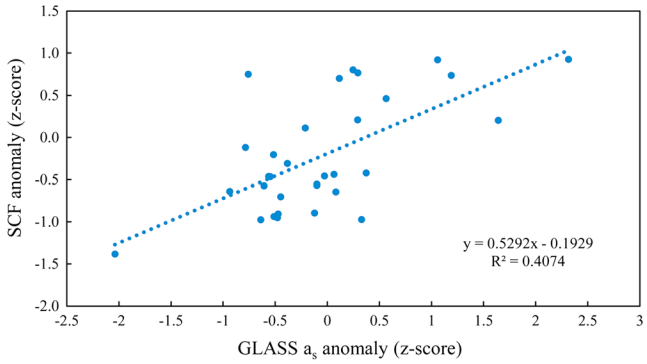

Figure A2. Linear correlation between the land surface albedo anomaly (*z*-score) and the SCF anomaly over the TP from 1982 to 2014.

influence the main conclusions of this study. Linear correlation between the land surface albedo anomaly (z-score) and the SCF anomaly over the TP from 1982 to 2014 are displayed in Figure A2. The interannual correlation between the SCF from the Northern Hemisphere EASE-Grid 2.0 Weekly Snow Cover and Sea Ice data set and land surface as derived from GLASS is highly correlated with R^2 being 0.41($p < 0.001$) over the TP from 1982 to 2014. Thus, changes in snow cover can be well represented by anomalies in a_s in the corresponding period.

Acknowledgments

The snow cover data used in this study are provided by the Northwest Institute of Eco-Environment and Resources, Chinese Academy of Sciences (http://westdc.westgis.ac.cn/data). The GLASS albedo products are provided by Beijing Normal University (http://glcf.umd.edu/data/abd/). The MCD43GF snow-free land surface albedo products are provided by the University of Massachusetts Boston Professor Crystal Schaaf's Lab (ftp://rsftp.eeos.umb.edu/data02/Gapfilled/); the CERES radiation budget data are available at https://ceres.larc.nasa.gov/order_data.php; the CAM radiative kernels are available at http://people.oregonstate.edu/~shellk/kernel.html. The GFDL kernels are available from http://www.rsmas.miami.edu/personal/bsoden/data/kernels.html, and streamflow observations are obtained upon request (dlong@tsinghua.edu.cn). This study was funded by the National Natural Science Foundation of China (under grants 91547210, 51579128, and 91437214) and China's Postdoctoral Science Foundation (under grant 2016M600080).

References

Arnell, N. W., and S. N. Gosling (2016), The impacts of climate change on river flood risk at the global scale, *Clim. Change*, *134*(3), 387–401, doi:10.1007/s10584-014-1084-5.

Boos, W. R., and Z. Kuang (2010), Dominant control of the South Asian monsoon by orographic insulation versus plateau heating, *Nature*, *463*(7278), 218–222, doi:10.1038/nature08707.

Brown, R., C. Derksen, and L. Wang (2010), A multi-data set analysis of variability and change in Arctic spring snow cover extent, 1967–2008, *J. Geophys. Res.*, *115*, D16111, doi:10.1029/2010JD013975.

Brown, R. D., and D. A. Robinson (2011), Northern Hemisphere spring snow cover variability and change over 1922–2010 including an assessment of uncertainty, *Cryosphere*, *5*(1), 219–229, doi:10.5194/tc-5-219-2011.

Cao, Y., S. Liang, X. Chen, and T. He (2015), Assessment of sea ice albedo radiative forcing and feedback over the Northern Hemisphere from 1982 to 2009 using satellite and reanalysis data, *J. Clim.*, *28*(3), 1248–1259, doi:10.1175/jcli-d-14-00389.1.

Chen, X., S. Liang, Y. Cao, T. He, and D. Wang (2015), Observed contrast changes in snow cover phenology in northern middle and high latitudes from 2001–2014, *Sci. Rep.*, *5*, 16820, doi:10.1038/srep16820.

Chen, X., S. Liang, and Y. Cao (2016a), Satellite observed changes in the Northern Hemisphere snow cover phenology and the associated radiative forcing and feedback between 1982 and 2013, *Environ. Res. Lett.*, *11*(8), 084002), doi:10.1088/1748-9326/11/8/084002.

Chen, X., S. Liang, Y. Cao, and T. He (2016b), Distribution, attribution, and radiative forcing of snow cover changes over China from 1982 to 2013, *Clim. Change*, *137*(3–4), 363–377, doi:10.1007/s10584-016-1688-z.

Chen, X., D. Long, Y. Hong, C. Zeng, and D. Yan (2017), Improved modeling of snow and glacier melting by a progressive two-stage calibration strategy with GRACE and multisource data: How snow and glacier meltwater contributes to the runoff of the Upper Brahmaputra River basin?, *Water Resour. Res.*, *53*, 2431–2466, doi:10.1002/2016WR019656.

Cohen, J., et al. (2014), Recent Arctic amplification and extreme mid-latitude weather, *Nat. Geosci.*, *7*(9), 627–637, doi:10.1038/ngeo2234.

Cohen, J. L., J. C. Furtado, M. A. Barlow, V. A. Alexeev, and J. E. Cherry (2012), Arctic warming, increasing snow cover and widespread boreal winter cooling, *Environ. Res. Lett.*, *7*(1), 014007), doi:10.1088/1748-9326/7/1/014007.

Derksen, C., and R. Brown (2012), Spring snow cover extent reductions in the 2008–2012 period exceeding climate model projections, *Geophys. Res. Lett.*, *39*, L19504, doi:10.1029/2012GL053387.

Dong, J., G. Zhang, Y. Zhang, and X. Xiao (2013), Reply to Wang et al.: Snow cover and air temperature affect the rate of changes in spring phenology in the Tibetan Plateau, *Proc. Natl. Acad. Sci. U.S.A.*, *110*(31), E2856–E2857, doi:10.1073/pnas.1306813110.

Duan, A., and Z. Xiao (2015), Does the climate warming hiatus exist over the Tibetan Plateau?, *Sci. Rep.*, *5*, 13711, doi:10.1038/srep13711.

Flanner, M. G., K. M. Shell, M. Barlage, D. K. Perovich, and M. A. Tschudi (2011), Radiative forcing and albedo feedback from the Northern Hemisphere cryosphere between 1979 and 2008, *Nat. Geosci.*, *4*, 151–155, doi:10.1038/NGEO1062.

Frei, A., M. Tedesco, S. Lee, J. Foster, D. K. Hall, R. Kelly, and D. A. Robinson (2012), A review of global satellite-derived snow products, *Adv. Space Res.*, *50*(8), 1007–1029, doi:10.1016/j.asr.2011.12.021.

Hall, A., X. Qu, and J. D. Neelin (2008), Improving predictions of summer climate change in the United States, *Geophys. Res. Lett.*, *35*, L01702, doi:10.1029/2007GL032012.

Hall, D. K., G. A. Riggs, and V. V. Salomonson (1995), Development of methods for mapping global snow cover using moderate resolution imaging spectroradiometer data, *Remote Sens. Environ.*, *54*(2), 127–140, doi:10.1016/0034-4257(95)00137-P.

Haynes, M. A., K.-J. S. Kung, J. S. Brandt, Y. Yongping, and D. M. Waller (2014), Accelerated climate change and its potential impact on Yak herding livelihoods in the eastern Tibetan Plateau, *Clim. Change*, *123*(2), 147–160, doi:10.1007/s10584-013-1043-6.

He, T., S. Liang, Y. Yu, D. Wang, F. Gao, and Q. Liu (2013), Greenland surface albedo changes in July 1981–2012 from satellite observations, *Environ. Res. Lett.*, *8*(4), 044043), doi:10.1088/1748-9326/8/4/044043.

Helfrich, S. R., D. McNamara, B. H. Ramsay, T. Baldwin, and T. Kasheta (2007), Enhancements to, and forthcoming developments in the Interactive Multisensor Snow and Ice Mapping System (IMS), *Hydrol. Processes*, *21*(12), 1576–1586, doi:10.1002/hyp.6720.

Huang, X., X. Hao, Q. Feng, W. Wang, and T. Liang (2014), A new MODIS daily cloud free snow cover mapping algorithm on the Tibetan Plateau, *Sci. Cold Arid. Reg.*, *6*(2), 0116–0123, doi:10.3724/SP.J.1226.2014.00116.

Intergovernmental Panel on Climate Change (2013), *Climate Change 2013: The Physical Science Basis. Contribution of Working Group I to the Fifth Assessment Report of the Intergovernmental Panel on Climate Change* edited by T. F. Stocker, et al., pp. 317–382, Cambridge Univ. Press, Cambridge, U. K., and New York, doi:10.1017/CBO9781107415324.

Kelly, R. E., A. T. Chang, L. Tsang, and J. L. Foster (2003), A prototype AMSR-E global snow area and snow depth algorithm, *IEEE Trans. Geosci. Remote Sens.*, *41*(2), 230–242, doi:10.1109/tgrs.2003.809118.

Kreyszig, E. (1979), *Advanced Engineering Mathematics*, 4th ed., pp. 1014–1015, Wiley, Jefferson City, Mo.

Larson, C. (2011), "Third pole" glacier research gets a boost from China, *Science*, *334*(6060), 1199, doi:10.1126/science.334.6060.1199.

Lau, W. K. M., M.-K. Kim, K.-M. Kim, and W.-S. Lee (2010), Enhanced surface warming and accelerated snow melt in the Himalayas and Tibetan Plateau induced by absorbing aerosols, *Environ. Res. Lett.*, *5*(2), 025204), doi:10.1088/1748-9326/5/2/025204.

Liang, S., X. Zhang, Z. Xiao, J. Cheng, Q. Liu, and X. Zhao (2013a), *Global LAnd Surface Satellite (GLASS) Products: Algorithms, Validation and Analysis*, pp. 33–72, Springer, New York, doi:10.1007/978-3-319-02588-9.

Liang, S., et al. (2013b), A long-term Global LAnd Surface Satellite (GLASS) data-set for environmental studies, *Int. J. Digital Earth*, *6*, 5–33, doi:10.1080/17538947.2013.805262.

Liu, J., and R. Chen (2011), Studying the spatiotemporal variation of snow-covered days over China based on combined use of MODIS snow-covered days and in situ observations, *Theor. Appl. Climatol.*, *106*(3–4), 355–363, doi:10.1007/s00704-011-0441-9.

Loeb, N. G., B. A. Wielicki, D. R. Doelling, G. L. Smith, D. F. Keyes, S. Kato, N. Manalo-Smith, and T. Wong (2009), Toward optimal closure of the Earth's top-of-atmosphere radiation budget, *J. Clim.*, *22*(3), 748–766, doi:10.1175/2008jcli2637.1.

Long, D., Y. Shen, A. Sun, Y. Hong, L. Longuevergne, Y. Yang, B. Li, and L. Chen (2014), Drought and flood monitoring for a large karst plateau in Southwest China using extended GRACE data, *Remote Sens. Environ.*, *155*, 145–160, doi:10.1016/j.rse.2014.08.006.

Long, D., Y. Pan, J. Zhou, Y. Chen, X. Y. Hou, Y. Hong, B. R. Scanlon, and L. Longuevergne (2017), Global analysis of spatiotemporal variability in merged total water storage changes using multiple GRACE products and global hydrological models, *Remote Sens. Environ.*, *192*, 198–216.

Ma, Y., L. Zhong, Z. Su, H. Ishikawa, M. Menenti, and T. Koike (2006), Determination of regional distributions and seasonal variations of land surface heat fluxes from Landsat-7 Enhanced Thematic Mapper data over the central Tibetan Plateau area, *J. Geophys. Res.*, *111*, D10305, doi:10.1029/2005JD006742.

Ma, Y., et al. (2009), Recent advances on the study of atmosphere-land interaction observations on the Tibetan Plateau, *Hydrol. Earth Syst. Sci.*, *13*, 1103–1111, doi:10.5194/hess-13-1103-2009.

Mölg, T., F. Maussion, and D. Scherer (2013), Mid-latitude westerlies as a driver of glacier variability in monsoonal High Asia, *Nat. Clim. Change*, *4*(1), 68–73, doi:10.1038/nclimate2055.

Moody, E. G., M. D. King, C. B. Schaaf, and S. Platnick (2008), MODIS-derived spatially complete surface albedo products: Spatial and temporal pixel distribution and zonal averages, *J. Appl. Meteorol. Climatol.*, *47*(11), 2879–2894, doi:10.1175/2008jamc1795.1.

Nie, J., et al. (2015), Loess Plateau storage of northeastern Tibetan Plateau-derived Yellow River sediment, *Nat. Commun.*, *6*, 8511, doi:10.1038/ncomms9511.

Pu, Z., L. Xu, and V. V. Salomonson (2007), MODIS/Terra observed seasonal variations of snow cover over the Tibetan Plateau, *Geophys. Res. Lett.*, *34*, L06706, doi:10.1029/2007GL029262.

Pu, Z., L. Xu, and V. V. Salomonson (2008), MODIS/Terra observed snow cover over the Tibet Plateau: Distribution, variation and possible connection with the East Asian Summer Monsoon (EASM), *Theor. Appl. Climatol.*, *97*(3–4), 265–278, doi:10.1007/s00704-008-0074-9.

Qu, X., and A. Hall (2014), On the persistent spread in snow-albedo feedback, *Clim. Dyn.*, *42*, 69–81, doi:10.1007/s00382-013-1774-0.

Robinson, D. A., K. F. Dewey, J. Richard, and R. Heim (1993), Global snow cover monitoring: An update, *Bull. Am. Meteorol. Soc.*, *74*, 1689–1696, doi:10.1175/1520-0477(1993)074<1689:GSCMAU>2.0.CO;2.

Shell, K. M., J. T. Kiehl, and C. A. Shields (2008), Using the radiative kernel technique to calculate climate feedbacks in NCAR's Community Atmospheric Model, *J. Clim.*, *21*(10), 2269–2282, doi:10.1175/2007jcli2044.1.

Shen, M., et al. (2015), Evaporative cooling over the Tibetan Plateau induced by vegetation growth, *Proc. Natl. Acad. Sci. U.S.A.*, *112*(30), 9299–9304, doi:10.1073/pnas.1504418112.

Soden, B. J., I. M. Held, R. Colman, K. M. Shell, J. T. Kiehl, and C. A. Shields (2008), Quantifying climate feedbacks using radiative kernels, *J. Clim.*, *21*(14), 3504–3520, doi:10.1175/2007jcli2110.1.

Tang, G., Y. Wen, J. Gao, D. Long, Y. Ma, W. Wan, and Y. Hong (2017), Similarities and differences between three coexisting spaceborne radars in global rainfall and snowfall estimation, *Water Resour. Res.*, *53*, 1–19, doi:10.1002/2016WR019961.

Wang, T., S. Peng, X. Lin, and J. Chang (2013), Declining snow cover may affect spring phenological trend on the Tibetan Plateau, *Proc. Natl. Acad. Sci. U.S.A.*, *110*(31), E2854–E2855, doi:10.1073/pnas.1306157110.

Wielicki, B. A., B. R. Barkstrom, E. F. Harrison, R. B. Lee III, G. Louis Smith, and J. E. Cooper (1996), Clouds and the Earth's Radiant Energy System (CERES): An Earth observing system experiment, *Bull. Am. Meteorol. Soc.*, *77*(5), 853–868, doi:10.1175/1520-0477(1996)077<0853:CATERE>2.0.CO;2.

Wu, Z., Z. Jiang, J. Li, S. Zhong, and L. Wang (2012), Possible association of the western Tibetan Plateau snow cover with the decadal to interdecadal variations of northern China heatwave frequency, *Clim. Dyn.*, *39*(9–10), 2393–2402, doi:10.1007/s00382-012-1439-4.

Yao, T., et al. (2012), Different glacier status with atmospheric circulations in Tibetan Plateau and surroundings, *Nat. Clim. Change*, *2*, 663–667, doi:10.1038/nclimate1580.

Zhang, G., Y. Zhang, J. Dong, and X. Xiao (2013), Green-up dates in the Tibetan Plateau have continuously advanced from 1982 to 2011, *Proc. Natl. Acad. Sci. U.S.A.*, *110*(11), 4309–4314, doi:10.1073/pnas.1210423110.

Zhang, Y., L. Tim, and W. Bin (2004), Decadal change of the spring snow depth over the Tibetan Plateau: The associated circulation and influence on the East Asian summer monsoon, *J. Clim.*, *17*, 2780–2793, doi:10.1175/1520-0442(2004)017<2780:DCOTSS>2.0.CO;2.

Zhong, L., Z. Su, Y. Ma, M. S. Salama, and J. A. Sobrino (2011), Accelerated changes of environmental conditions on the Tibetan Plateau caused by climate change, *J. Clim.*, *24*(24), 6540–6550.